Journal of Zhejiang University-SCIENCE A (Applied Physics & Engineering) in press
www.jzus.zju.edu.cn; www.springer.com/journal/11582
E-mail: jzus_a@zju.edu.cn

Research Article

https://doi.org/10.1631/jzus.A2400345

Dynamic response of the ground beneath a high-speed railway based on typical upper Shanghai clays involving water table change

Jing HU[1]✉, Chengming YE[1], Juntao JIANG[1], Shujing WU[1], David THOMPSON[2], Xuecheng BIAN[3]

[1]*College of Civil Engineering, Fuzhou University, Fuzhou 350108, China*
[2]*Institute of Sound and Vibration Research, University of Southampton, Highfield, Southampton SO17 1BJ, UK*
[3]*MOE Key Laboratory of Soft Soils and Geoenvironmental Engineering, Department of Civil Engineering, Zhejiang University, Hangzhou 310058, China*

Abstract: A rising water table increases soil water content, reduces soil strength, and amplifies vibrations under identical train loads, thereby posing greater risks to train operations. To investigate this phenomenon, we used a 2.5D finite element model (FEM) of a coupled vehicle-embankment-ground system based on Biot's theory. The ground properties were derived from a typical soil profile of the Yangtze River basin, using geological data from Shanghai. The findings indicate that a rise in the water table leads to increased dynamic displacements of both the track and the ground. This amplification effect extends beyond the depth of the water table, impacting the entire embankment-foundation cross-section, and intensifies with higher train speeds. However, the water table rise has a limited impact on the critical speed of trains and dominant frequency contents. The dynamic response of the embankment is more significantly affected by water table rises within the subgrade than by those within the ground. When the water table rises into the subgrade, significant excess pore pressure is generated inside the embankment, causing a substantial drop in effective stress. As a result, the stress path of the soil elements in the subgrade approaches the Mohr-Coulomb failure line, increasing the likelihood of soil failure.

Key words: Dynamic response; Excess pore pressures; Water table rise; High-speed train; 2.5D FEM

1 Introduction

Compared to traditional railways, high-speed trains (HSTs) induce significant track-ground vibrations, increasing train operational risks. This issue is particularly serious when trains approach critical speeds, causing a resonant-like effect (Madshus and Kaynia, 2000; Costa et al., 2015; Hu et al., 2019). Simultaneously, the frequency of extreme rainstorms has risen globally, increasing groundwater storage in upper soil layers (Huang et al., 2021). For example, Southeast China experienced an increase of 3.799 billion m^3 in groundwater storage within the Yangtze River basin between 2019 and 2020, raising the shallow water table by 0.5 to 2.0 m (Huang et al., 2021). The dynamic behaviour of the track-ground system is closely related to the soil properties of the embankment and foundation. A rising water table increases soil water content, reduces soil strength (Duong et al., 2013), and amplifies vibrations under the same train load (Jiang et al., 2016; Hu et al., 2023). Additionally, excess pore pressure in the soil alters stress distribution, thereby posing greater threats to train operations. To mitigate these risks and support the demand for faster trains, studying the dynamic response of high-speed railways in relation to changes in the water table is essential.

Several studies have directly measured the dynamic responses and deformation of railway embankments under different water tables through large-scale model tests. Jiang et al. (2016) established a full-scale physical model of a ballastless track and studied the dynamic responses of the embankment as the water table rose from the bottom to the surface. They found that the vibration response of the embankment increased significantly due to the rise in groundwater level. Other full-scale physical model investigations by Huang et al. (2018) and Chen et al. (2014) drew similar conclusions.

Constructing large-scale model testing equipment is often both challenging and costly. As a

✉ Jing HU, jingh@fzu.edu.cn
Jing HU, https://orcid.org/0000-0003-0495-2749

Received July 16, 2024; Revision accepted Nov. 26, 2024;

result, researchers frequently use analytical and semi-analytical methods to study wave characteristics in saturated foundations under moving loads. Some of the studies on the dynamic response of porous media are summarized in Fig. 1. Notably, most current research relies on linear elastic models. Although natural soil behavior is generally nonlinear, the stress within embankments remains mainly within the elastic strain range due to the strength of artificial fill materials. Furthermore, stress diffusion in the embankment results in a ground foundation stress typically below 10 kPa (Hu and Bian, 2022). Thus, even in natural soil, stress levels largely stay within the elastic range, making linear elasticity theory a reasonable approach for analyzing the dynamic response of saturated foundations.

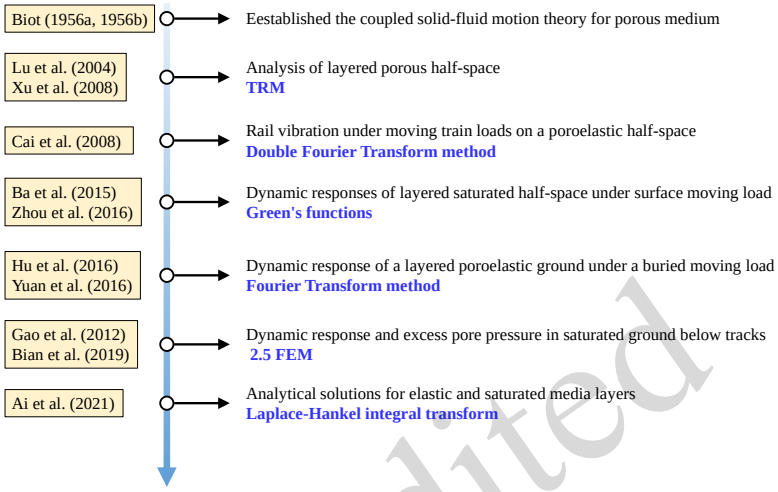

Fig. 1. Brief summary of studies on the dynamic response of porous media

For high-speed railways, the track structure's consistent geometry and material properties along the longitudinal direction have led some researchers to apply the 2.5-dimensional finite element method (2.5D FEM) to analyze dynamic responses (Gao et al., 2012a, 2014b; Hu and Bian, 2022). Bian et al. (2019) and Hu et al. (2021) established 2.5D FEM models of a high-speed railway embankment on a saturated foundation to investigate the effects of the saturated soil permeability coefficient and train speed on the dynamic response. Despite significant advancements in computational efficiency, existing finite element methods are still based mainly on constitutive models of single-phase media, and dynamic solutions for saturated media remain limited.

A rise in water table induces a transition in some foundation and embankment soil from an approximate single-phase state with minimal water content to a saturated state. Consequently, considerations regarding water table rise entail addressing key issues such as multi-layer soil dynamics and the transformation of certain soil layers from a single-phase to a saturated medium. To date, analytical methods have encountered challenges in solving dynamic problems involving multi-layered saturated media. Additionally, existing 2.5D FEM models treat the foundation mainly as entirely saturated soil, overlooking variations in the water table within both the foundation and embankment.

To address these deficiencies, we propose the establishment of a 2.5D FEM model that combines single-phase and saturated media. The rise of the water table is simulated by transitioning from a single-phase to a saturated medium. Considering that the Yangtze River basin hosts some of the world's largest and busiest HST lines, a representative soil layer from Shanghai was used to exemplify the foundation characteristics in this region. Subsequently, the dynamic response of the railway embankment and foundation under HST loads was simulated for a variable water table, ranging from within the foundation to the surface of the embankment. We examined the effects of water table rise on dynamic displacement, excess pore pressure, and effective stress.

2 Typical upper Shanghai clays

Shanghai is not only one of the largest and most

prosperous cities in the world, it is also at the heart of the Yangtze River basin in China. Due to numerous underground projects over the last few decades, the engineering properties of Shanghai upper clays have been extensively studied (Dassargues et al., 1991; Schroeder et al., 1992; Ng et al., 2011). From a geological perspective, upper Shanghai clay is part of the modern Yangtze River basin, and thus its geological characteristics can be taken as broadly representative of the area. The Quaternary soil layer in Shanghai can be divided into upper and lower parts according to the different sedimentary components of the soil layer. The lower part is early Pleistocene continental sedimentary soil, with a buried depth of generally more than 145 m, and is an interlayer of clay and gray-white sand (Wu, 2016.). The upper part, which is relevant to modern engineering construction, is deposited where the marine environment had gradually advanced following frequent infringements since the Middle Pleistocene period. Its buried depth is less than 145 m, and it is an interlayer of clay, light gray and yellow-gray sand (Wu, 2016; Yan and Shi, 2006.). More specifically, in the range down to 70 m below the surface, it consists mainly of loose sediments of marine facies formed by the alternation of sea and land since the Middle Pleistocene (Wu, 2016.). In other words, this part of the stratum is interdeposited with soft clay and sand, layer by layer. According to the sedimentation of the modern Yangtze River basin since the mid-Holocene (Dassargues et al., 1991), upper Shanghai clays can be divided approximately into six layers (Fig. 2) (Bai, 2014; Shui et al., 2014). These can be identified as: ① crust layer, ② first sand layer, ③ first compression layer, ④ second sand layer, ⑤ second compression layer and ⑥ first hard soil layer. Based on the above geological conclusions and the division of the engineering geological and hydrogeological districts of upper Quaternary Shanghai soil layers reported by Dassargues et al. (1991) and Wu (2016), a simplified layering of typical foundation soil for upper Shanghai clays was selected (Fig. 3).

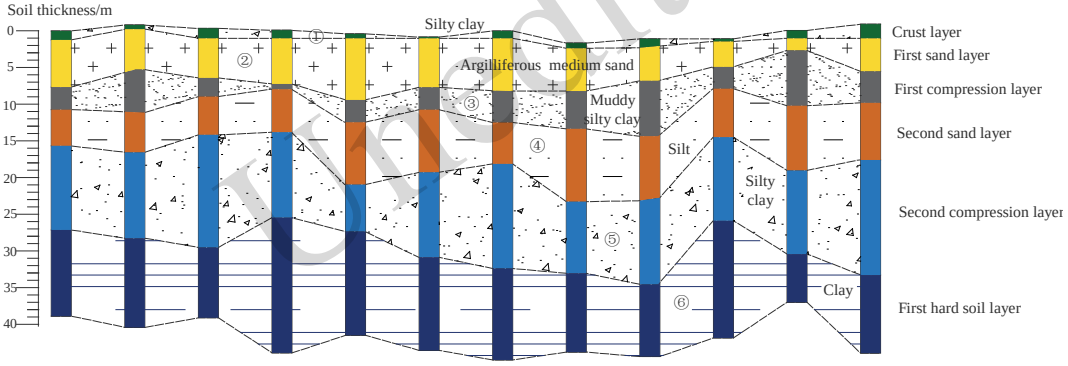

Fig. 2. Schematic view of a typical soil layer distribution of upper Shanghai clays

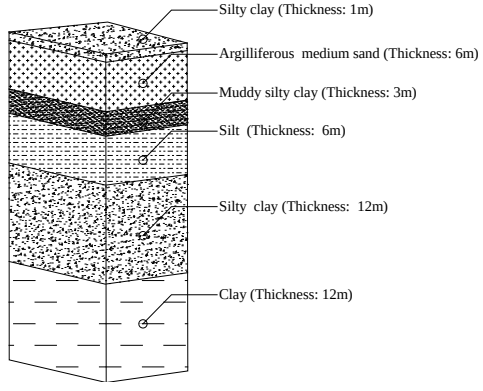

Fig. 3. Simplified representation of foundation soil layers for upper Shanghai clays

3 Introduction of the semi-analysis solution method and numerical model

3.1 Brief introduction of the semi-analysis solution method

The widely adopted governing equations of Biot (1956a, 1956b) are use to describe the motion of embankments and ground under moving train loads. Given that the track geometry and properties of high-speed railways remain consistent longitudinally, the dynamic response of both track and ground under moving train loads can be analyzed in the wavenumber domain. This approach enables the use of a 2.5D finite element method to compute responses

across the entire 3D space by evaluating responses in a 2D section for various wavenumbers. Detailed derivation procedures have been extensively documented (Gao et al., 2012; Bian et al., 2019).

Regarding changes in the water table, the region above it is treated as a single-phase medium. Fig. 4 describes the two-phase saturated medium and single-phase medium in the 2.5D FEM model, where k_x represents the wavenumber along the x direction, α and M are the Biot constants, ρ_f is the density of the pore fluid, n is the porosity, m is the effective density, and k_D is the soil permeability coefficient. For single-phase media, setting the liquid phase parameters close to zero is sufficient (Hu, et al., 2023). Subsequently, a 2.5D FEM saturated element can effectively model the behavior of single-phase mediums.

3.2 2.5D finite element model

Fig. 5 depicts the 2.5D finite element model of the embankment and ground, where the total model depth is 42.7 m and width is 100 m. Using symmetry, the model includes only 50 m. The embankment stands at a height of 2.7 m, including a 0.4 m roadbed layer and a 2.3 m subgrade layer. The soil layers in the foundation replicate upper Shanghai clays, detailed in Fig. 2. The embankment and soil layers are represented by 2.5D saturated linear elastic elements with 6 degrees of freedom per node. In the model, the embankment and foundation surfaces are free, while the left, right, and bottom boundaries are fixed. To prevent wave reflection within the finite element domain, a multi-layer damped boundary is implemented, as successfully demonstrated by Bian et al. (2019). The model includes three layers of damping on the left, right, and bottom sides, respectively. A nominal damping loss factor of 0.05 was assigned to the ground to avoid numerical issues. Moving outward from the inner part of the model, the damping values for each layer are 0.1, 0.2, and 0.4, respectively.

Four observation points, labelled A through D, are marked in Fig. 5. Point A is located at the surface of the embankment (z = 0 m), point B at the surface of the subgrade (z = 0.4 m), point C at the ground surface (z = 2.7 m) and point D at 1.7 m beneath the ground surface (z = 4.4 m). As indicated in Fig. 5, ten different water tables were considered in this study. The water table was taken to rise gradually from the bottom of the sand layer, by 1 m between each case from the initial state to Case 6. Within the subgrade, three water levels were considered, with a rise of 0.8 m between them, up to the subgrade surface.

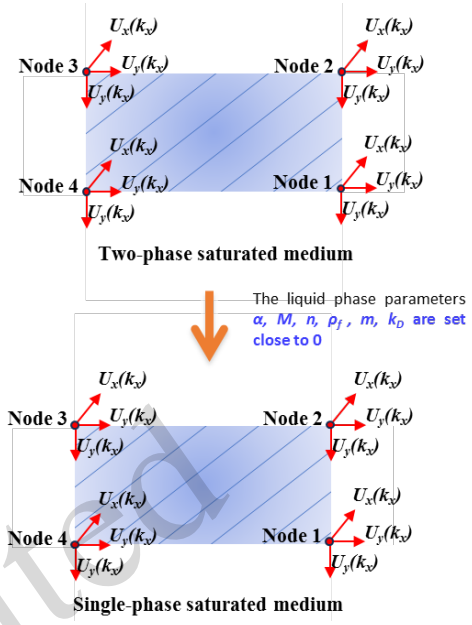

Fig. 4. Description of the two-phase saturated medium and single-phase medium in the 2.5 D FEM model

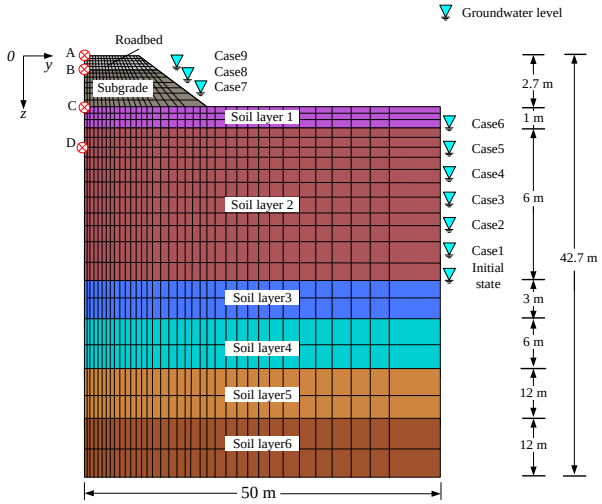

Fig. 5. Schematic view of numerical model (not to scale)

3.3 Model validation

Jiang et al. (2016a) constructed a full-scale model of a slab track-embankment system designed for Chinese high-speed railways. This physical model was used to assess the dynamic performance of the track-embankment system under various typ-

ical water tables. In this section, measurements of vibrations at the embankment surface were selected from the saturated foundation and saturated subgrade cases to validate the 2.5D FEM model. Table 1 lists the parameters of the full-scale physical model before and after changes in the water table. Only the saturated foundation and saturated subgrade cases were simulated. The values in Table 1 are mostly referenced from Jiang et al. (2016b).

As depicted in Fig. 6, the vibration velocities of the embankment surface calculated by the 2.5D FEM were compared with the results from model tests. The comparison shows that across train speeds ranging from 1 to 100 m/s, the results from the 2.5D finite element calculations align closely with the test results. This validation underscores the accuracy of the 2.5D finite element model.

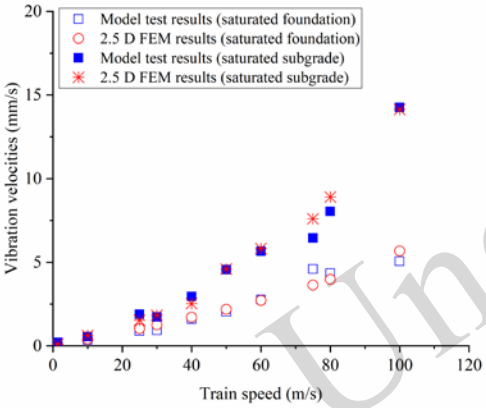

Fig. 6. Verification of the 2.5D element method via model test results

3.4 Relevant properties for numerical analysis

According to geological investigations, most of the natural soil layers are normally in a high state of saturation; even the sand layer can have a saturation of about 70%. In the model, the embankment and foundation were therefore simulated by saturated media. Specifically, soil layer 2, the argilliferous medium sand layer, is represented in the initial state by a saturated element with a small permeability coefficient and a large modulus. As the water table rises, its permeability coefficient is increased, and its modulus reduced (Mualem, Y.,1976). In this way, a change of the water table is introduced in this layer. Soil layer 1, the silty clay, is assumed not to change with the rise of water table. For the embankment, its initial state is an approximate single-phase state, thus the parameters α, M, n, ρ_f and k_D, were set close to 0, which means no water is contained in the embankment. The initial values of the soil materials for each layer are listed in Table 2. Since the water table changes only within the subgrade and argilliferous medium sand layer, the values for these two layers after water table rise are listed in Table 3. The parameters in both Table 2 and Table 3 are based on typical values from geological survey reports (Dassargues et al., 1991; Schroeder et al., 1992; Wu, 2016; Yan and Shi, 2006).

Table 1 Parameters of the full-scale physical model before/after a water table rise

Layer number	Layer name	α	M (MPa)	Young's modulus E (MPa)	Poisson's ratio v	ρ_s (kg/m^3)	ρ_f (kg/m^3)	Porosity n	Permeability coefficient k_D (m/s)
Embankment	Roadbed	0.001	0.001	240	0.25	2200	0.001	0.001	10^{-20}
	Subgrade (before)	0.001	0.001	140	0.3	2000	0.001	0.001	10^{-20}
	Subgrade (after)	1	6400	80	0.3	2700	1000	0.3	6×10^{-4}
Soil layer 1-6	Qiantang Silty	1	3520	45	0.35	2700	1000	0.6	1×10^{-6}

Table 2 Parameters for a typical Shanghai upper layer at initial state

Layer number	Layer name	α	M (MPa)	Young's modulus E (MPa)	Poisson's ratio v	ρ_s (kg/m^3)	ρ_f (kg/m^3)	Porosity n	Permeability coefficient k_D (m/s)
Embankment	Roadbed	0.001	0.001	240	0.25	2200	0.001	0.001	10^{-20}
	Subgrade	0.001	0.001	140	0.28	2000	0.001	0.001	10^{-20}

Soil layer 1	Silty clay	1	3930	23	0.33	2730	1000	0.53	2.93×10^{-8}
Soil layer 2	Argilliferous medium sand	1	6570	55	0.3	2600	1000	0.29	1.6×10^{-4}
Soil layer 3	Muddy silty clay	1	3140	6.4	0.35	2600	1000	0.68	2×10^{-9}
Soil layer 4	Silt	1	4540	36	0.34	2700	1000	0.45	6×10^{-6}
Soil layer 5	Silt clay	1	4140	21	0.33	2730	1000	0.5	8.86×10^{-8}
Soil layer 6	Clay	1	4540	38	0.33	2740	1000	0.45	9.36×10^{-9}

Table 3 Parameters after water table rise

Soil layer	α	M (MPa)	Young's modulus E (MPa)	Poisson's ratio v	ρ_s (kg/m^3)	ρ_f (kg/m^3)	Porosity n	Permeability coefficient k_D (m/s)
Subgrade	1	6400	80	0.28	2000	1000	0.3	6×10^{-4}
Argilliferous medium sand	1	6570	39	0.3	2730	1000	0.42	2.4×10^{-4}

Table 4 shows the track parameters used in the simulation (Bian et al., 2019). The numerical simulation incorporated vehicle loads based on a six-car CRH2 train, using a quarter car model (Takemiya and Bian, 2005). The axle load is 144 kN. The specific parameters of the CRH2 are detailed in Table 5 (Bian et al., 2019).

Table 4 Parameters of slab track

Rail mass per unit length (kg/m)	Rail bending stiffness (MNm^2)	Track slab bending stiffness (MNm^2)	Mass per unit length of track slab (kg/m)
60.64	6.625	40	950
Bending stiffness of concrete base (MNm^2)	**Mass per unit length of concrete base (kg/m)**	**Fastener stiffness (MN/m/m)**	**Fastener damping (Ns/m/m)**
190	1800	28.5	5×10^4

Table 5 Parameters used for the CRH2 train

Carriage mass (kg)	Bogie mass (kg)	Wheelset mass (kg)	Carriage length (m)	Centre-to-centre distance of adjacent bogies (m)	Bogie length (m)
45000	3600	1700	24.8	14.9	2.5

4 Numerical analysis

4.1 Vibration responses

Fig. 7 illustrates the time-history curves of vibration displacement at point A on the embankment surface under different water tables, corresponding to train speeds of 30 and 70 m/s.

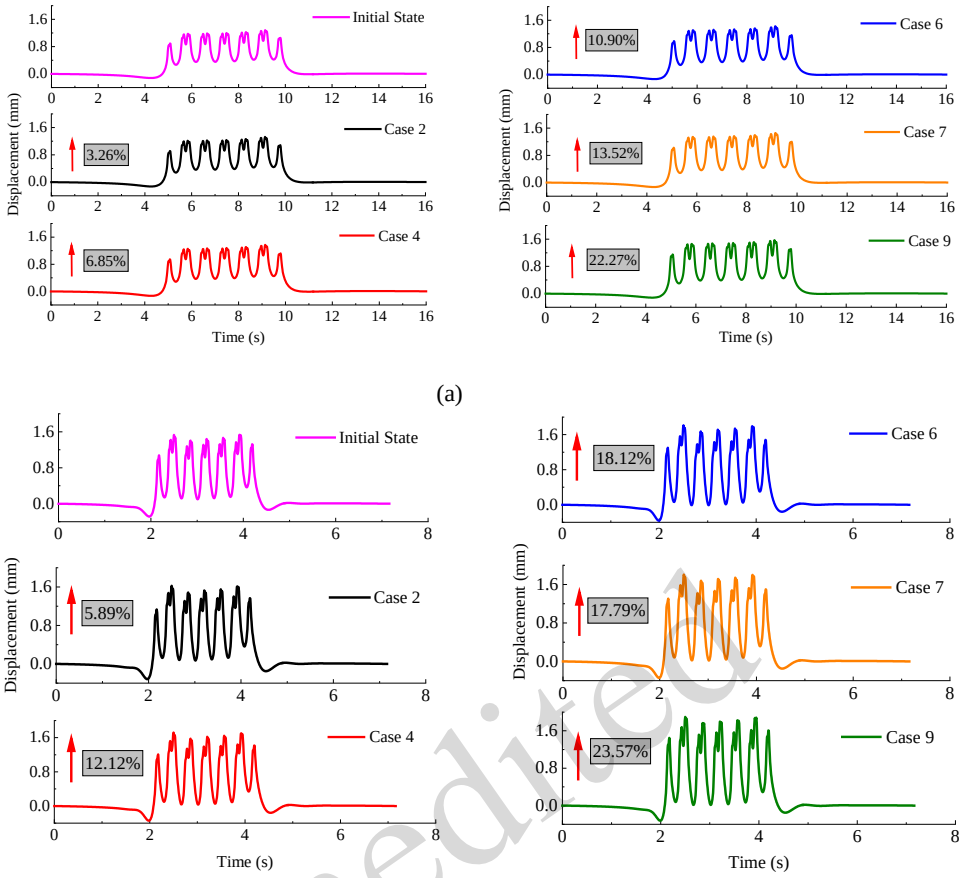

Fig. 7. Time-history curves of vibration displacement at point A (z = 0 m) under various cases and different train speeds: (a) 30 m/s; (b) 70 m/s

In Fig. 7(a), it is evident that at a speed of 30 m/s, the shape of the dynamic displacement time-history curve at point A remains consistent across different water table conditions. As the water table rises from its initial state to Case 9, the maximum displacement at point A increases from 1.30 to 1.57 mm. The percentage increases in maximum displacement for each case are also shown in the figure. The rise in the water table within the subgrade notably affects the dynamic response of the embankment more than when the water table rise is confined to the underlying ground. At a train speed of 70 m/s (Fig. 7 (b)), the percentage increases in dynamic displacement for each case are similar to, or slightly higher than, those observed at 30 m/s. It is clear that the increase in water table leads to a significant rise of up to 23.57% in dynamic displacement, regardless of whether the train operates at low or high speeds.

Fig. 8 shows the percentage increase in displacement as a function of depth for each case, under train speeds of 30 m/s and 70 m/s. Fig. 8 reveals that the displacement amplitude consistently increases compared to the initial state, demonstrating an amplification effect throughout the cross-section of both the embankment and ground due to changes in the water table. The increase in displacement response from rising water tables also affects regions below the new water table, with the greatest amplification occurring near the water table, particularly noticeable from Case 1 to Case 6. The depth-wise distribution shows more variability from Case 7 to Case 9, influenced mainly by the interfaces between different layers near the altered water table. Comparing Figs 8(a) and (b), it is evident that the overall amplification effect intensifies with increasing train speed.

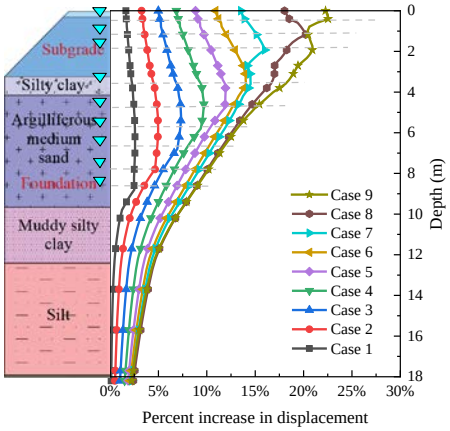

(a)

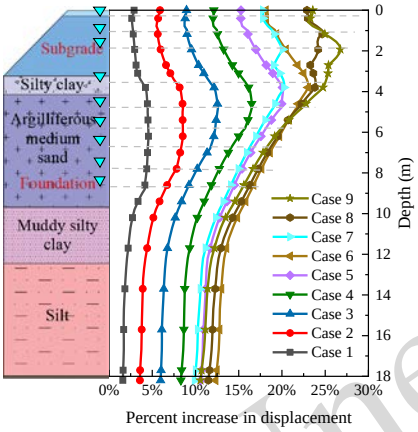

(b)

Fig. 8. Percentage increases in dynamic displacement for each case plotted against depth: (a) 30 m/s; (b) 70 m/s

Fig. 9 illustrates the evolution of maximum displacement responses at point A (z = 0 m) and point C (z = 2.7 m) as a function of train speed. At point C, the maximum response in each case is consistently smaller than at the surface.

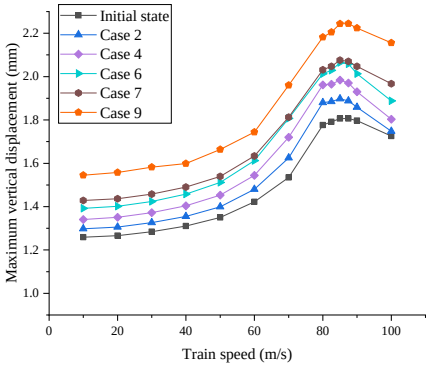

(a) Point A

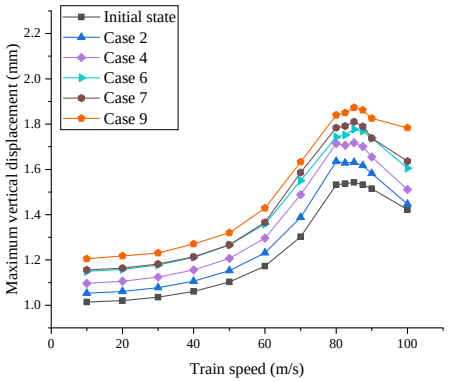

(b) Point C

Fig. 9. Dependence of maximum displacement responses on train load speeds for different depths and cases: (a) Point A; (b) Point C

Fig. 9 (a) shows that for a high-speed railway constructed on typical upper Shanghai clays, the critical speed of the entire embankment-ground system in its initial state is about 87.5 m/s (315 km/h), which corresponds to the speed with the largest displacement amplitude. There are minimal variations in speed between 80 and 90 m/s across different water table cases. With an increase in water table, the critical speed of the system shows slight variation, decreasing marginally to 85 m/s. A similar trend is observed in Fig. 9(b) regarding the maximum displacement responses of the foundation.

Considering the initial critical speed of around 90 m/s for the entire embankment-ground system, we conducted frequency analysis of vibrations at a train speed of 90 m/s. Fig. 10 presents the frequency contents of vibration displacement at point A (z = 0 m) and point C (z = 2.7 m).

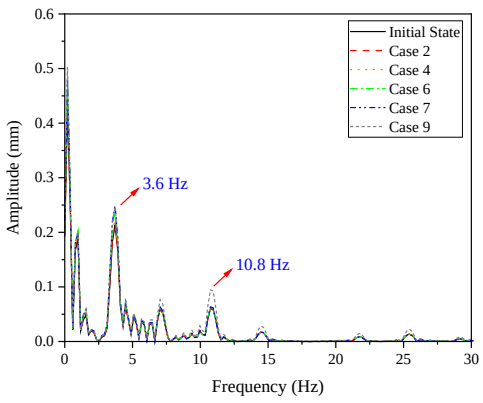

(a) Point A

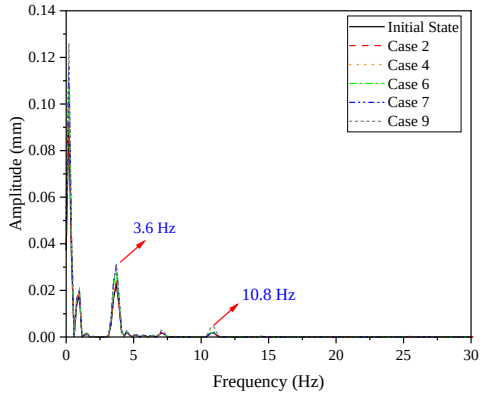

(b) Point C

Fig. 10. Frequency spectrum analysis of the vibration displacement under a train speed of 90 m/s

Fig. 10 depicts the frequency content data, highlighting peaks at about 3.6 Hz and 10.8 Hz, along with their higher-order harmonic frequencies, observed at a train speed of 90 m/s. These dominant frequencies correspond to the passage of train carriages and individual bogies at the ends of coupled carriages, as discussed by Priest et al. (2010) and Bian et al. (2014). Importantly, these dominant frequencies remain consistent across different water tables for both the subgrade and ground foundation. However, the amplitude increases with the water table. These findings are consistent with measurement results of Jiang et al. (2016a). Moreover, a notable increase in amplitude in the frequency domain is observed as the water table rises within the subgrade. Another observed phenomenon is that, as depth increases, the amplitude of the vibration response in the frequency domain decreases rapidly. Additionally, different water table levels show slight variations in the rate of amplitude reduction, with a 90% decrease for the initial state and an 87% decrease when the water table rises to the subgrade.

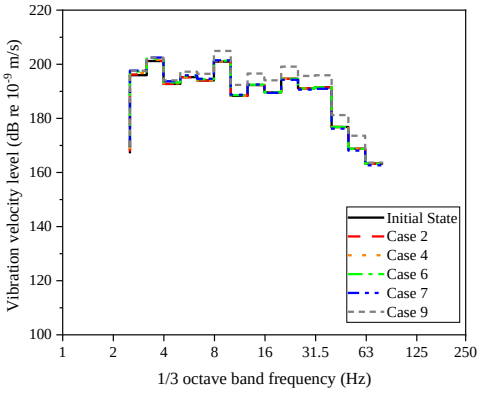

(a)

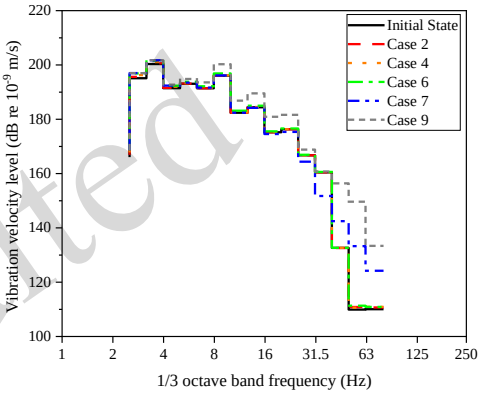

(b)

Fig. 11. 1/3 octave band frequency analysis under a train speed of 90 m/s: (a) Point A; (b) Point C

Fig. 11 presents the 1/3 octave band frequency analysis at a speed of 90 m/s, based on vibration data from the subgrade surface. The analysis shows peak vibration velocities from 3.2 to 4.0 Hz and 8.0 to 10.0 Hz, attributed by the length of the train carriage and the adjoining bogies. Additionally, while there is a slight increase in vibration velocity as the water table rises in the ground, a significant increase is observed when the water table changes within the subgrade. The frequency range of peak vibration remains unchanged with increasing depth but the intensification caused by a rising water table becomes increasingly evident. In the foundation, once the water table reaches the subgrade, the vibration amplitudes at high frequencies (greater than 31.5 Hz) in Case 7 and Case 9 show quite significant increases.

4.2 Excess pore pressure responses

Fig. 12 shows the vertical distribution of maximum excess pore pressure for different cases, including the initial state, for train speeds of 30 m/s and 70 m/s. The maximum excess pore pressures exhibit a complex dependence on depth due to the variable permeabilities of the multi-layered foundation. For the initial state and Cases 1 to 6, the subgrade is treated as a single-phase medium, resulting in zero excess pore pressures. The silty clay layer has low soil permeability, leading to an increase in excess pore pressure. In contrast, the argilliferous medium sand layer has a much higher permeability, causing a decreasing trend in excess pore pressure within this layer. Near the bottom of the argilliferous medium sand layer, the presence of the muddy silty clay layer with lower permeability causes a slight increase in excess pore pressures with depth. Below the muddy silty clay layer, the excess pore pressure decreases to nearly zero due to the significant distance from the load.

Table 6 lists the peak values of excess pore pressure and their locations for each case at different train speeds. For the initial state at a train speed of 30 m/s, the peak excess pore pressure is 4.69 kPa, located in the silty clay layer at a depth of 3.6 m. As the water table rises in the argilliferous medium sand layer, its increased permeability results in a decrease in peak pore pressure values and a shallower depth at which the maximum value occurs. At a higher train speed of 70 m/s, this trend of decreasing peak values and their depths slows down. The deeper deformation depth caused by higher speed trains ensures that the peak excess pore pressure remains in the silty clay layer at a depth of 3.6 m, even in Case 7, when the water table rises to the subgrade. At higher train speeds, the peak excess pore pressure tends to appear deeper, with Case 9 showing a greater peak value. This could raise concerns about deformation in the deeper soft foundation soil. For both speeds, it is notable that in Case 9, with the water table rising significantly into the subgrade, substantial excess pore pressures are generated in the subgrade.

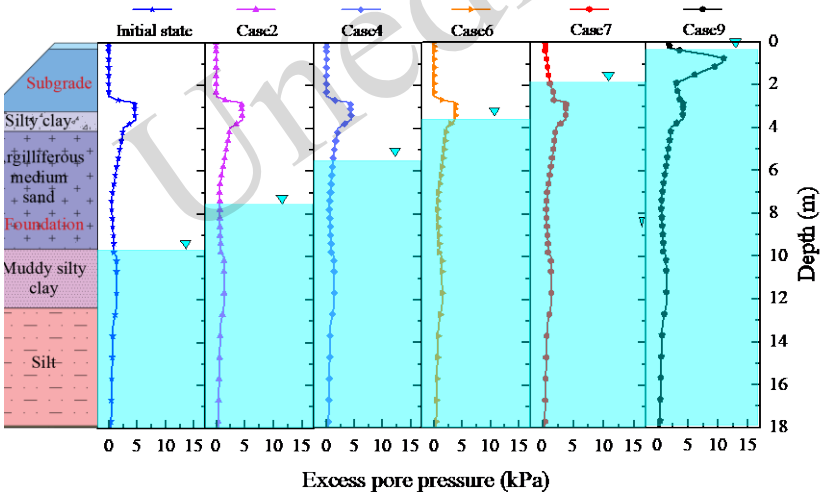

(a)

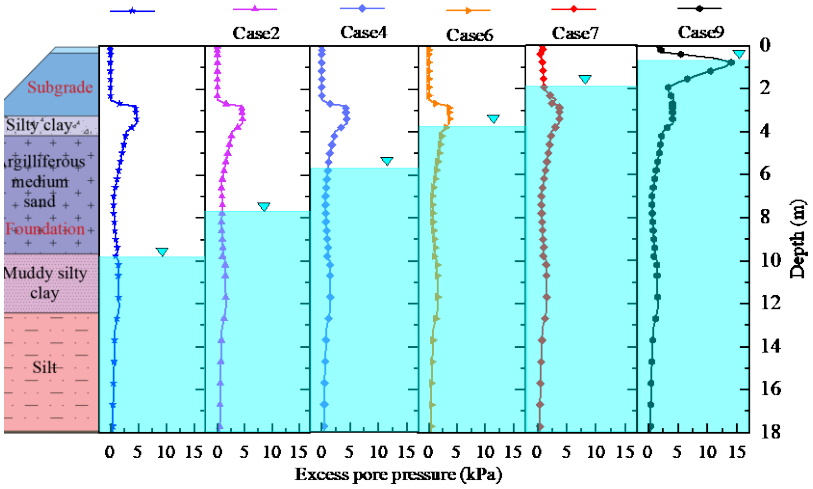

(b)

Fig. 12. Maximum excess pore pressures versus depth: (a) 30 m/s; (b) 70 m/s

Table 6 Peak excess pore pressures in different cases and their locations

	30 m/s		70 m/s	
Case	Peak excess pore pressure (kPa)	Location (m)	Peak excess pore pressure (kPa)	Location (m)
Initial State	4.69		4.79	
Case 2	4.61	3.6	4.68	
Case 4	4.41		4.46	3.6
Case 6	3.83		3.70	
Case 7	3.98	2.8	3.77	
Case 9	10.97	0.78	13.97	0.78

Fig. 13 illustrates the distribution of maximum excess pore pressure responses in a cross-section of both the embankment and ground (*y*-*z* plane) at a train speed of 70 m/s, about 0.8 times the embankment-ground system's critical speed, for the initial state and Case 9. To facilitate comparison of the size of the affected area in different cases, areas where the excess pore pressure exceeds 3 kPa are highlighted in red. The maximum values are indicated in the figures.

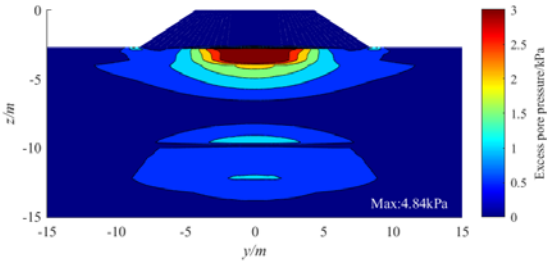

(a) Initial state

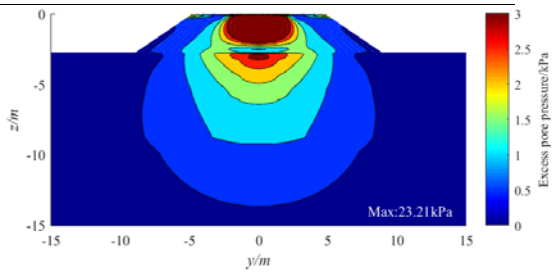

(b) Case 9

Fig. 13. Excess pore pressure distribution contours of different cases in the *y*-*z* plane at 70 m/s

In Fig. 13(a), the excess pore pressure is concentrated near the ground surface, peaking at about 4.84 kPa in the silty clay layer, with a parabolic distribution below this layer. Additionally, there is a region where the excess pore pressure exceeds 0.5 kPa at depths between 9 and 14 m. In Case 9, which features the highest water table, significant excess pore pressure extends across a considerable portion of the subgrade, forming an elliptical distribution. In this case, the maximum excess pore pressure is signifi-

cantly higher, reaching about 23.2 kPa.

4.3 Effective Stress Analysis

Fig.14 plots the stress paths at point B, the top of the subgrade, under two different cases and for train speeds of 30 m/s and 70 m/s. The graph presents p (=[σ_1-σ_3]/2) against q (=[σ_1+σ_3]/2), where p is the mean principal stress, q is the mean deviating stress, σ_1 is maximum principal stress, and σ_3 is the minimum principal stress. They are based on a coefficient of lateral earth pressure $K_0 = 0.5$. According to Duong et al. (2013), the internal friction angle φ of the nearly saturated embankment material is 29°, and its cohesion c is 21 kPa. An indicative Mohr-Coulomb failure line is also shown for reference. It is important to note that this failure line is included purely for illustrative purposes: since the analyses in this paper used purely elastic soil models, even if the stress path reaches the line, it does not imply soil failure.

Fig. 14 reveals that as the water table ascends to the surface of the subgrade, the stress path curve at point B shows a significant deflection towards the indicative Mohr-Coulomb failure line. This deviation becomes more pronounced with increasing train speed, bringing the stress path closer to the failure line. This suggests that both a rising water table and higher train speeds increase the likelihood of soil failure in the subgrade.

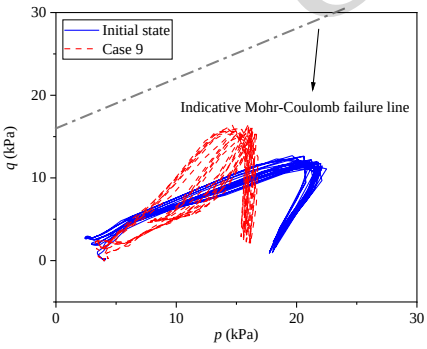

(a) 30m/s

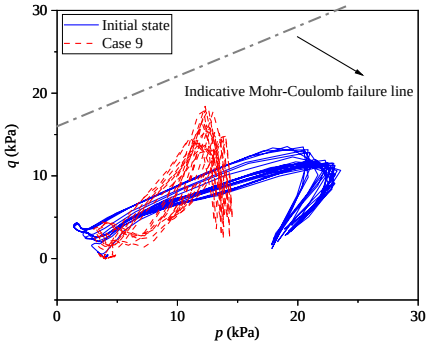

(b) 70m/s

Fig. 14. Effective stress path at point B under different train speeds: (a) 30 m/s; (b) 70 m/s

Fig. 15 shows the contour distribution of effective stress responses under a train speed of 70 m/s, for the initial state and Case 9. The effective stress reaction within the embankment is concentrated mainly in the impact zone of the train wheels and gradually diffuses as depth increases.

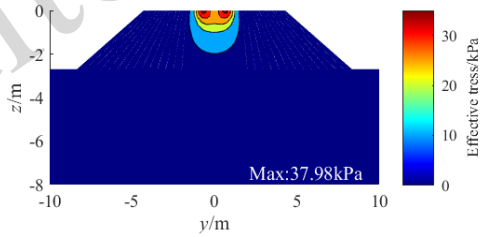

(a) Initial state

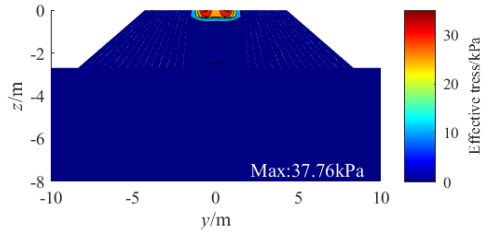

(b) case 9

Fig. 15. Contours of maximum effective stress for different cases in the *y*-*z* plane at 70 m/s

In the initial state, the effective stress response in the *y*-*z* plane exhibits a smooth parabolic distribution, tapering down to 5 kPa at the base of the subgrade. For Case 9, with the highest water table, the effective stress response follows an approximately cylindrical distribution, diminishing to 5 kPa near the subgrade surface. A comparison of these two states reveals that the rise in the water table within the subgrade leads to a rapid drop in effective stress with increasing depth,

significantly increasing the susceptibility to subgrade instability.

5 Summary and conclusions

The increase in rainfall attributed to global warming has led to a rise in water table within subgrades and foundations, subsequently altering their dynamic behavior under train loads. Traditional analytical and numerical methods face significant challenges when addressing dynamic problems involving multi-layered saturated media and soil phase transformation. To address these challenges, in this paper we propose a 2.5D FEM model that integrates both single-phase and saturated media. The model simulates the rise in water table by transitioning from a single-phase to a saturated medium. This study uses a representative soil layer from Shanghai to exemplify the foundation characteristics prevalent in the Yangtze River basin. The main findings of this study are as follows:

1. The rise in the water table amplifies the track's dynamic displacement. This increase in displacement amplitude is not confined to the depth of the water table change but affects the entire embankment-foundation cross-section. This amplification effect intensifies with higher train speeds.

2. For a high-speed railway built on typical upper Shanghai clays, the critical speed is around 85 m/s. While the rise in the water table significantly increases the displacement amplitude, it has minimal impact on the critical speed.

3. The vibration frequency of the embankment and foundation is influenced mainly by the length of the train carriage and the adjoining bogies. These dominant frequencies remain consistent across different water tables for both the subgrade and the ground foundation. However, the amplitude of these frequencies increases with the water table. Notably, there is a significant increase in amplitude when the water table rises within the subgrade.

4. Generally, the rise in the water table within the foundation decreases the peak values of excess pore pressure and the depth at which the maximum values occur. However, at higher train speeds, these decreasing trends slow down. The higher the train speed, the deeper the position at which the peak excess pore pressure appears. When the water table rises within the subgrade, the peak values of excess pore pressure increase.

5. The rise in the water table within the subgrade has a more pronounced effect on the dynamic response of the embankment than on the ground foundation. When the water table rises into the subgrade, significant excess pore pressure is generated within the embankment. This condition brings the stress path closer to the indicative Mohr-Coulomb failure line, increasing the likelihood of soil failure in the subgrade.

6. The rise in the water table within the subgrade causes the effective stress to drop rapidly with increasing depth, reducing the soil's capacity and increasing the susceptibility to subgrade instability.

Acknowledgments

Financial support has been received from the National Natural Science Foundation of China (Grant No.52108308), and the National Key Research and Development Program Young Scientist Project (Grant No.2024YFC2911000).

Author contributions

Jing HU and Xuecheng BIAN designed the research. Jing HU and David THOMPSON processed the corresponding data. Jing HU wrote the first draft of the manuscript. Chengming YE and Juntao JIANG helped to organize the manuscript. Shujing WU revised and edited the final version.

Conflict of interest

Jing HU, Chengming YE, Juntao JIANG, Shujing WU, David THOMPSON, and Xuecheng BIAN declare that they have no conflict of interest.

References

Ai ZY, Ji WT, Li Y, et al., 2021. Dynamic response of saturated multilayered soils with elastic superstrata subjected to vertical impulsive loadings. Applied Mathematical Modelling, 91:875-891. http://dx.doi.org/10.1016/j.apm.2020.09.019.

Ba ZN, Liang JW, Jin W, 2015. Dynamic response of coupled system of track and layered fliud-saturated ground under moving high-speed loads. Engineering Mechanics, 32:189-200. (in Chinese). DOI: 10.6052/j.issn.1000-4750.2014.04.0323

Bai, TH, 2014. New Technologies Applied in Design and Construction of Shanghai Metro Works. Tunnel Construction, 34(1):53-59.(in Chinese).

Bian XC, Hu J, Thompson, D., et al., 2019. Pore pressure generation in a poro-elastic soil under moving train loads. Soil Dynamics and Earthquake Engineering, 125. http://dx.doi.org/10.1016/j.soildyn.2019.105711.

Biot MA, 1956. Theory of propagation of elastic waves in a fluid-saturated porous solid. I. low-frequency range. Journal of the Acoustical Society of America, 28:168-178. http://dx.doi.org/10.1121/1.1908239.

Biot MA, 1956. Theory of propagation of elastic waves in a fluid-saturated porous solid. II. higher frequency range. Journal of the Acoustical Society of America, 28:179-191. http://dx.doi.org/10.1121/1.1908241.

Cai YQ, Sun HL, Xu CJ, 2008. Response of railway track system on poroelastic half-space soil medium subjected to a moving train load. International journal of Solids and Structures, 45:5015-5034. http://dx.doi.org/10.1016/j.ijsolstr.2008.05.002.

Chen RP, Zhao X, Jiang HG., et al., 2014. Model test on deformation characteristics of slab. Journal of the China railway society, 36:87-93.(in Chinese).

Costa PA, Colaço A, Calçada R, et al., 2015. Critical speed of railway tracks. Detailed and simplified approaches. Transportation Geotechnics, 2:30-46. https://doi.org/10.1016/j.trgeo.2014.09.003

Dassargues A., Biver P, Monjoie A, 1991. Geotechnical properties of the Quaternary sediments in Shanghai. Engineering Geology, 31:71-90. http://dx.doi.org/10.1016/0013-7952(91)90058-S.

Duong TV, Tang AM, Cui YJ, et al., 2013. Effects of fines and water contents on the mechanical behavior of interlayer soil in ancient railway sub-structure. Soils and Foundations, 53(6). https://doi.org/10.1016/j.sandf.2013.10.006.

Gao GY, Chen GQ, Li J, 2014. Numerical analysis of dynamic characteristic of transversely isotropic saturated soil foundation subjected to high-speed train load. Chinese Journal of Rock Mechanics and Engineering, 33:189-198. (in Chinese).

Gao GY, Chen QS, He J, Liu F, 2012. Investigation of ground vibration due to trains moving on saturated multi-layered ground by 2.5D finite element method. Soil Dynamics and Earthquake Engineering, 40:87-98. https://doi.org/10.1016/j.soildyn.2011.12.003.

Hu AF, LI YJ, Jia YS, et al., 2016. Dynamic response of a layered saturated ground subjected to a buried moving load. Engineering Mechanics, 33(12):44-51. (in Chinese). DOI: 10.6052/j.issn.1000-4750.2015.04.0275

Hu J, Bian X, 2022. Experimental and numerical studies on dynamic responses of tunnel and soils due to train traffic loads. Tunnelling and Underground Space Technology, 128:104628. https://doi.org/10.1016/j.tust.2022.104628.

Hu J, Bian X, Xu W, et al., 2019. Investigation into the critical speed of ballastless track. Transportation Geotechnics, 18:142-148. https://doi.org/10.1016/j.trgeo.2018.12.004

Hu J, Bian XC, 2022. Analysis of dynamic stresses in ballasted railway track due to train passages at high speeds. Journal of Zhejiang University-SCIENCE A, 23:443-457.

Hu J, Jin LL, Wu SJ, et al., 2023. Effect of water tablerise on the critical velocity of high-speed railway. Water, 15(21):3764. https://doi.org/10.3390/w15213764.

Hu J, Tang Y, Zhang JK, et al., 2021. Dynamic responses of saturated soft soil foundation under high speed train. Rock and Soil Mechanics, 42:3169-3181. (in Chinese).

Huang CS, Zhou Y, Zhang SN, et al., 2021. Groundwater resources in the Yangtze river basin and its current development and utilization. Geology in China, 48(4):979-1000. (in Chinese). DOI: 10.12029/gc20210401

Huang JJ, Su Q, Wang W, et al., 2018. Field investigation and full-scale model testing of mud pumping and its effect on the dynamic properties of the slab track–subgrade interface. Proceedings of the Institution of Mechanical Engineers, Part F: Journal of Rail and Rapid Transit, 233:802-816. http://dx.doi.org/10.1177/0954409718810262.

Jiang HG, Bian XC, Jiang JQ, et al., 2016a. Dynamic performance of high-speed railway formation with the rise of water table. Engineering Geology, 206:18-32. http://dx.doi.org/10.1016/j.enggeo.2016.03.002.

Jiang HG, Bian XC, Cheng C, et al., 2016b. Simulating train moving loads in physical model testing of railway infrastructure and its numerical calibration[J]. Acta Geotechnica, 11: 231-242. https://doi.org/10.1007/s11440-014-0327-y

Lu JF, Hanyga A, 2004. Fundamental solution for a layered porous half space subject to a vertical point force or a point fluid source. Computational Mechanics, 35:376-391. https://doi.org/10.1007/s00466-004-0626-5.

Madshus CC, Kaynia AM, 2000. High-speed railway lines on soft ground: dynamic behaviour at critical train speed. Journal of Sound and Vibration, 231:689-701. https://doi.org/10.1006/jsvi.1999.2647

Mualem, Y. 1976. A new model for predicting the hydraulic conductivity of unsaturated porous media. Water resources research, 12(3), 513-522. https://doi.org/10.1029/WR012i003p00513

Ng C, Li Q, Liu G, 2011. Characteristics of one-dimensional compressibility of Shanghai clay. Chinese Journal of Geotechnical Engineering, 33:630-636. (in Chinese).

Schroeder C, Dassargues A, Li XL, 1992. Engineering geological conditions in the central area of Shanghai. Bulletin of the International Association of Engineering Geology, 46:37-43. http://dx.doi.org/10.1007/BF02595031.

Shui LS, Huai NW, Yu JC, et al., 2014. Long-term settlement behaviour of metro tunnels in the soft deposits of Shanghai. Tunnelling and Underground Space Technology, 40:309-323. https://doi.org/10.1016/j.tust.2013.10.013.

Takemiya H, Bian XC, 2005. Substructure simulation of inhomogeneous track and layered ground dynamic interaction under train passage. Journal of Engineering Mechanics, 131:699-711. https://doi.org/10.1061/(ASCE)0733-9399(2005)131:7(699).

Wu CJ, 2016. Depositional Environment and Geotechnical

Properties for the Upper Shanghai Clays. PhD Thesis, Shanghai Jiao Tong University, Shanghai, China. (in Chinese).

Xu B, Lu JF, Wang, JH, et al., 2008. Dynamic response of layered saturated soil under moving loads. Rock and Soil Mechanics, 29:3186-3192.(in Chinese).

Yan XX, Shi YJ, 2006. Structure characteristic of engineering geology in Shanghai. Shanghai Geology, 4:19-24.(in Chinese).

Yuan ZH, Cai YQ, Cao ZH, 2016. An analytical model for vibration prediction of a tunnel embedded in a saturated full-space to a harmonic point load. Soil Dynamics and Earthquake Engineering, 86:25-40. https://doi.org/10.1016/j.soildyn.2016.04.004.

Zhou SH, Hen C, Di HG, 2016. Dynamic 2.5-D green's function for a poroelastic half-space. Engineering Analysis with Boundary Elements, 67:96-107. http://dx.doi.org/10.1016/j.enganabound.2016.03.011.

中文概要

题　目：基于上海典型地层的水位抬升下高铁路基动力响应研究

作　者：胡静[1],叶成名[1],江俊涛[1],吴淑婧[1],David THOMPSON[2]，边学成[3]

机　构：[1]福州大学，土木工程学院，中国福州，350108；[2]南安普顿大学，声学与振动研究所，英国南安普顿，SO17 1BJ；[3]浙江大学，软弱土与环境土工教育部重点实验室，中国杭州，310058

目　的：本研究旨在探讨地下水水位抬升对车辆-路基-地基系统动力响应的影响。研究主要聚焦于水位抬升如何改变路基和地基在列车荷载下的振动位移，有效应力和超静孔压，分析水位抬升高度和列车运行速度对路基-地基动力响应及路基失稳风险的具体影响。

创新点：1. 调研和收集了大量上海的地质信息和数据，建立了具有代表性的上海典型地层和水位抬升模型；2. 建立了多层多相介质的 2.5 维有限元模型，获得了不同地下水位条件下的动力响应。

方　法：1. 通过文献调研，建立了上海典型地层；2. 基于 Biot 理论建立了多相介质动力问题的 2.5 维有限元求解方法，通过改变单元参数，实现水位抬升的模拟；3. 围绕列车速度、水位抬升高度进行数值模拟，揭示了水位抬升对路基/地基动力响应的影响。

结　论：1. 水位抬升使得路基-地基的振动强度增大，这种振动强度的放大作用并不是局限在水位变化的深度范围内，而是会导致整个路基和地基断面的振动增大，并且这种全断面式的振动放大效应随着列车速度的提高而增强；2. 上海典型地层上建造的高速铁路，其临界速度大约为 85 m/s，水位抬升虽然显著增加了位移响应，但对临界速度的影响很小；3. 水位抬升使得路基和地基频域内的响应幅值增大，特别是当水位抬升至路基时，幅值增加最为显著；4. 水位抬升不仅加剧了土体的变形，还会使饱和土体内出现超静孔压，有效应力减小；这会导致土单元上的剪应力与有效应力比值增大，进一步造成显著的土体变形；当水位抬升至路基内部时，路基内部出现显著的超静孔压，导致有效应力大幅下降，路基内土单元的应力路径向破坏线靠近，不利于路基的稳定。

关键词：动力响应；超静孔压；水位抬升；高速铁路；2.5 维有限元

==========